SXT Calibration Note # 34
Solar Physics 1995, 157, 141-168

The Point Spread Function of the Soft X-ray Telescope Aboard Yohkoh [1]

Petrus C. Martens
Space Science Dept., ESA/ESTEC
P.O. Box 299, 2200 AG Noordwijk
The Netherlands

Loren W. Acton
Dept. of Physics, Montana State University
Bozeman, MT 59717, U.S.A.

James R. Lemen
Lockheed Palo Alto Research Laboratory, Org. 91-30, Bldg. 252
3251 Hanover Street, Palo Alto, CA 94304-1121, U.S.A.

[1] This paper is dedicated to the memory of our friend and colleague Kermit Smith, who died in June 1993, after a valient fight with leukemia

Abstract

The point spread function of the SXT telescope aboard Yohkoh has been measured in flight configuration in three different X-ray lines at White Sands Missile Range. We have fitted these data with an elliptical generalization of the Moffat function. Our fitting method consists of χ^2 minimization *in Fourier space*, especially designed for matching of sharply peaked functions. We find excellent fits with a reduced χ^2 of order unity or less for single exposure point spread functions over most of the CCD. Near the edges of the CCD the fits are less accurate due to vignetting. From fitting results with summation of multiple exposures we find a systematic error in the fitting function of the order of 3% near the peak of the point spread function, which is close to the photon noise for typical SXT images in orbit.

We find that the the full width to half maximum and fitting parameters vary significantly with CCD location. However, we also find that point spread functions measured at the same location are consistent to one another within the limit determined by photon noise. A "best" analytical fit to the PSF as function of position on the CCD is derived for use in SXT image enhancement routines.

As an aside we have found that SXT can determine the location of point sources to about a quarter of a 2.54 arcsec pixel.

1. Introduction

The Japan/US/UK mission called Yohkoh (Japanese for "sunbeam") was launched on 31 August 1991 for the study of solar activity and flares (Ogawara, *et al.* 1991). The Yohkoh Soft X-ray Telescope (SXT) was prepared by a U.S.-Japan team for high resolution time-lapse imagery in X-rays. The SXT is a grazing-incidence reflecting telescope of 1.5 meter focal length that employs a 1024×1024 format virtual-phase CCD as a sensor. It has been described in detail by Tsuneta *et al.* (1991) and in references therein.

Initial calibration of the point spread function (PSF) of the SXT mirror was carried out in the 1000 foot x-ray calibration facility at Marshall Space Flight Center, AL. These tests revealed the mirror – the first high resolution X-ray mirror to be fabricated with both elements on a single substrate of Zerodur – to have excellent low-scatter and imaging properties. Each mirror element has a gold-coated hyperboloidal figure (Nariai, 1987, 1988) which gives better off-axis imaging performance than a Wolter-I mirror, although at the expense of on-axis resolution. The test techniques and results have been published by Lemen *et al.* (1989).

The design compromises dictated by the mission caused the SXT image to be under sampled. The CCD pixel size (2.45 arcseconds) is only slightly smaller than the core diameter of the PSF of the mirror. The best angular resolution of the telescope is in the 10-20 Å spectral range. For longer wavelengths the image is broadened by diffraction and at shorter wavelengths by mirror scatter. To extract the most information possible from the SXT solar images it is vital that the PSF of the telescope be well characterized.

We have learned from in-flight data that the far (X-ray scattering) wings of the PSF fall off as the inverse square of the distance from a bright image feature beyond about 20 arcseconds (Hara *et al.*, 1994). It is the purpose of this paper to provide a definitive description of the PSF of the SXT images for the core and near wings, as a function of wavelength and position in the focal plane. These data were obtained with the flight hardware at White Sands Missile Range, NM, just 4 months prior to launch.

2. The White Sands Tests

Final calibration of the SXT was accomplished at the High Energy Laser System Test Facility (HELSTF) at White Sands, New Mexico. The HELSTF is a cryogenically pumped vacuum system comprising a 300 m long pipe connected to a large, clean, experiment chamber. The SXT was mounted in the chamber on a digitally controlled pointing platform permitting independent motion in elevation and azimuth – with a step size of about 0.24 seconds of arc.

A microfocus X-ray source with a changeable target, manufactured by the Manson

Corp., and appropriate beam filtration was used to produce nearly monochromatic X-rays at one end of the long pipe. The X-ray spot subtended an angle of about 2/3 of an arcsecond from the position of the SXT. The most useful X-ray emission lines for our purposes were the K-lines of carbon (0.28 keV) and aluminum (1.49 keV) and the L-lines of silver (3.0 keV). The spectrum and intensity of the X-ray beam was monitored continuously during data acquisition with a thin-window proportional counter. The system was baffled to prevent scattered or reflected X-rays from reaching the monitor counter or the SXT focal plane.

A specialized Hartmann test was used to determine the position of best focus of the SXT for an on-axis source (Lemen *et al.*, 1989). The flight position of the CCD is 100 micrometers forward of this position – in order to provide a more uniform angular resolution across the 42 arcminute field of view of the telescope. The measurements presented in this paper were taken at the flight position, adjusted for the finite distance of the HELSTF source.

Following the setting of the focus, data were acquired in a highly automated manner for resolution and sensitivity calibration of the SXT. Positioning of the pointing platform, CCD exposure and readout, dark signal subtraction, recording of proportional counter rate and pulse height spectrum, file formatting and recording with a complete descriptive header and file name was all done under computer control. Data were reduced and checked in near real time to assure success. For the PSF calibration two types of files were prepared and are discussed in this paper. These were single-exposure *bx*-files and summed, multiple-exposure *sd*-files – for better statistical precision.

We believe that the results of this calibration provide an accurate representation of the resolution of the SXT in orbit. It is possible that gravitational distortion of the SXT mirror might play a role in the azimuthal assymetries observed in these results (e.g. Fig. 6) even though structural analysis indicates that that the effect should be very small. In any case, this is a second order effect of little significance for data analysis.

3. Least Squares Fit with Photon Statistics

The CCD for the Yohkoh Soft X-ray Telescope measures the number of free electrons produced in each pixel after the impact of an X-ray photon. The analog result is divided by the camera gain factor, *gf*, a constant set to prevent saturation in the 12 bit analog to digital converter. This yields the so-called Data Number (*DN*). For the WSMR tests the gain factor is 100, and in orbit it is approximately 90 to 100. It requires 3.65 eV to produce an electron-hole pair in silicon, and the number of produced electrons per photon is therefore the photon energy divided by 3.65 eV. For the White Sands tests a microfocus X-ray source with different targets yielding emission in three characteristic X-ray lines was used. These lines are: Al-K at 8.34 Å, C-K at 44.7 Å, and Ag-L at 4.16 Å.

Using X-ray lines has the advantage that the photon energy is narrowly determined, and hence that the number of incident photons can be determined quite accurately from the *DN*. The photon energy in keV for each line is found from $E = 12.40/\lambda$, where λ is the photon wavelength in Angströms. This leads to the following equation relating photon count N to Data Number *DN*,

$$N = 2.94 \times 10^{-4} \times DN \times \lambda \times gf. \tag{1}$$

Given the photon count per pixel, derived from the test results with Eq. (1), the uncertainty in each pixel count is simply the square root of the photon count, as is well known from photon statistics. Hence we can now assign a *weight* ($w_{n,m}$) to the photon count in each pixel, for fitting the test data with an analytical function. Statistical weight is usually defined as the inverse of the square of the uncertainty (e.g. Bevington 1969, p. 73), and hence for photon counts the simple result is,

$$w_{n,m} = 1/N_{n,m}. \tag{2}$$

This result implies that pixels with *zero* photon count would have infinite accuracy – a numerical impossibility that we avoided by adding a constant to the background subtracted image that sets the minimum count to one. Thus we also avoided negative photon counts (resulting from the subtraction of the average background) that would have negative weights and hence would reduce the total χ^2.

The statistical "best" fit of an analytical function $F_{n,m}$ with a test result $\mathrm{PSF}_{n,m}$ is obtained for those values of the parameters of the function F for which the weighted sum (χ^2) of the squares of the differences between the "fit" and the data is minimized, i.e.

$$\frac{\partial}{\partial a_i}\chi^2 = \frac{\partial}{\partial a_i}\sum_{n=-M}^{M}\sum_{m=-M}^{M} w_{n,m}[PSF_{n,m} - F(\vec{a})_{n,m}]^2 = 0, \tag{3}$$

where the a_i are the elements of the parameter vector $\vec{a}$, and where it has been assumed that the fitting takes place on a square lattice of $(2M+1) \times (2M+1)$ pixels.

An efficient numerical algorithm for minimizing χ^2 with respect to variations in the parameter vector (Eq. 3), using the gradient-expansion method, is described in Bevington, 1969, Chap. 11. We have used the IDL version of this program, *curvefit*, available from the IDL user-library, in all subsequent numerical fittings.

The goodness of a fit is usually characterized by the *reduced* χ^2, (χ^2_ν), determined by

$$\chi^2_\nu = \chi^2/\nu, \tag{4}$$

where ν is the number of degrees of freedom, defined as number of elements on the lattice (here $(2M+1)^2$) minus the size of the parameter vector (7+1 for the elliptical Moffat function plus background, see Sect. 4).

In summary, we determine best fits between analytical test functions and the White Sands measurements by the method of minimizing χ^2, assigning weights according to photon statistics. However, it will be shown in the following that the best fits are obtained by fitting the Fourier transform of the PSF, instead of the PSF itself. First we will describe the analytical function used for those fits.

4. The Elliptical Moffat Function

The Moffat function has been used to fit density spectra of globular clusters (Bendinelli, 1991). We derive a generalized version that provides an acceptable fit to the SXT point spread function measured at White Sands.

The original Moffat function is rotationally symmetric with regard to its maximum,

$$G(r) \;=\; \frac{c}{[1+(r/a)^2]^b}, \tag{5}$$

where r is the distance from the peak, and a, b, and c are parameters. For PSFs the parameters a and b are primary, because they determine the form of the Moffat function, while c is secondary, measuring only the peak photon count, which is proportional to the exposure time.

The White Sands PSF measurements indicate that the SXT PSF is in general not rotationally symmetric, but appears elliptical near the edges of the CCD. We have expanded the definition of the Moffat function to account for this lack of symmetry. The elliptical Moffat function is still given by Eq. (5), but the "radius" r is now defined by

$$r^2 \;=\; x^2(1+\varepsilon-\varepsilon_x) \,+\, y^2(1+\varepsilon+\varepsilon_x) \,-\, 2\varepsilon_y xy. \tag{6}$$

This expression defines a function with elliptical contours oriented along axes determined by the parameters ε_x, and ε_y, and with ε defined as $\varepsilon \;=\; \sqrt{\varepsilon_x^2+\varepsilon_y^2}$. The angle θ between the x-coordinate axis and the major axis of the ellips (in the usual counterclockwise direction) is given by

$$\theta = \frac{1}{2}\,\mathrm{arctan}(\varepsilon_y/\varepsilon_x), \tag{7}$$

where the π ambiguity in the *arctan* is of no consequence, since the axis extends in both directions.

We note that the Moffat function is a continuous analytical function, while the measured PSFs are sampled and digitized functions – one digital reading at every pixel. The comparison between the measured PSFs and the Moffat function is made by sampling the value of the Moffat function once in every pixel. The error introduced by comparing the digital PSF with the continuous value of the elliptical Moffat function is negligible compared to the uncertainty due to photon statistics, and will be ignored.

We denote the CCD coordinates of the pixel with the maximum X-ray intensity with x_{max} and y_{max}. Since there is no need for the peak of the Moffat function to be located exactly at the center of the pixel with the maximum of the PSF, the position of the Moffat function on the CCD is defined by,

$$x = x_n - x_{max} - x_c \quad \& \quad y = y_m - y_{max} - y_c, \tag{8}$$

where x_n and y_m are the CCD coordinates of the pixel centers, which are integers when the distance unit is the pixel distance, and x_c and y_c are the offset of the maximum of the Moffat function with regard to the peak pixel of the PSF.

We conclude this section by summarizing the parameters for the functional fit to the White Sands PSFs: a and b determine the form of the Moffat function, c merely measures the exposure time, while ε_x and ε_y form a vector whose size and direction determine the elliptical deformation of the modified Moffat function. Finally the vector x_c, y_c measures the off-set of the maximum of the Moffat function from the center of the peak pixel. To this we add an arbitrary constant bg, the background, which allows for uniform photon counts due to large-scale scatter and for a dark current. Fig. 1 shows a typical example of an elliptical Moffat function plus background.

5. Fitting in Fourier Space

We have tried several functional fits with the method described in Section 3. We fitted the observed PSFs with a skewed Moffat function in which the the contours are circles with increasing offset as r increases, with a Gaussian, and a function given by 1/r $\times$ Gaussian (see Lemen *et al*, 1989), with an appropriate cut-off in the limit r approaching zero, and, finally with the elliptical Moffat function of the previous section. To this we added, for all functions, a uniform background. For each of the functions we noticed the same problem: the result of the fitting procedure depends strongly on the size of the lattice used, expressed in the choice for the parameter M in Eq. (3). As M increases well beyond the FWHM of the measured PSFs, their fitting parameters, as well as χ^2_ν, keep on changing considerably. Moreover, visual comparison between the PSFs and their fits often shows very unsatisfactory results: around the peak of the PSF, where one would like the fit to be best, the fit often appears very poor.

The reason for these results becomes readily evident upon considering the nature of the χ^2 minimization procedure. This method is designed for functions that vary smoothly: the weight function depends on the uncertainties in such a way that the contribution to the summation in χ^2 (Eq. (3)) is of order unity *for each pixel.* However, the PSFs are sharply peaked functions – by definition the most sharply peaked image that can be obtained by the instrument. Therefore the method is not suitable for PSFs, in which many pixels represent irrelevant background, since the background pixels will still contribute equally

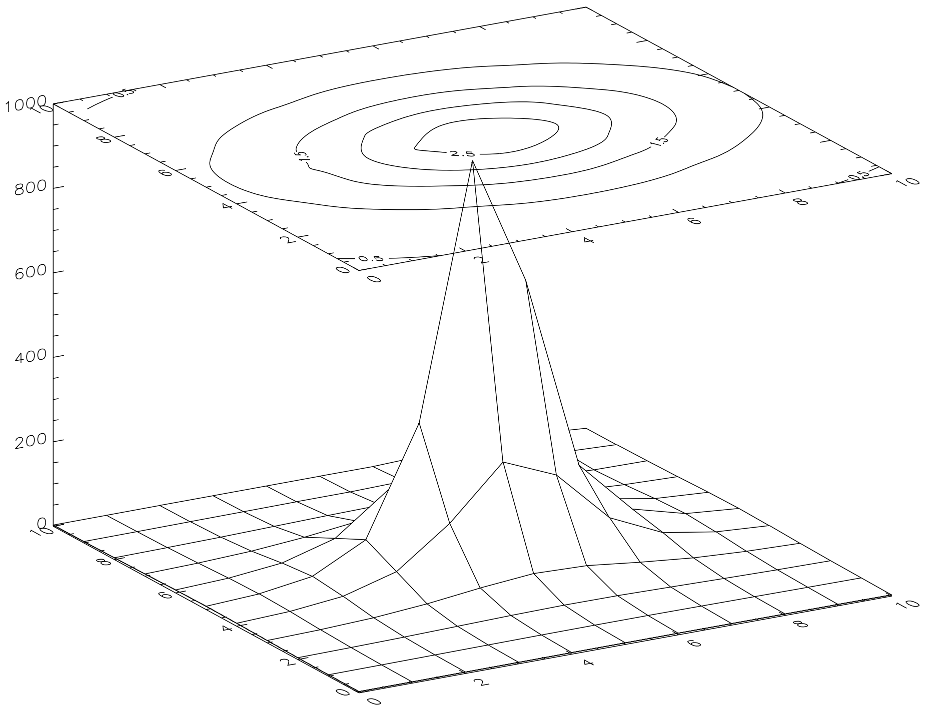

Figure 1. An example of the elliptical Moffat function defined in the text. The surface- and contour-plot are centered on an 11×11 matrix, and the parameter values used are: $a = 1.5$, $b = 2.0$, $c = 1000$, $x_c = 0.25$, $y_c = 0.0$, $\varepsilon_x = 0.5$, $\varepsilon_y = 0.0$, and $bg = 2.0$.

to χ^2, and spoil the fit. We tested this numerically by fitting a PSF simulated from a Gaussian with a Gaussian fitting function. The result was, as anticipated, that the fits for the broad Gaussians – i.e. functions for which the FWHM is comparable to the lattice length – are good, while the fit deteriorates as the FWHM is chosen smaller.

Since the Fourier transform of a sharply peaked function is a very broad function, a better fitting procedure may be fitting the Fourier transform of the PSF, known as the *Optical Transfer Function (OTF).* This is most easily seen by considering a Gaussian $\exp(-\alpha r^2)$, whose Fourier transform is also a Gaussian, $\pi^2/\alpha^2 \exp(-\pi^2 k^2/\alpha)$, with k denoting the magnitude of the wave-vector. As α increases the original Gaussian becomes more sharply peaked, while its Fourier transform becomes broader and broader. In the extreme case, the Fourier transform of a delta function is a constant. Thus, for sharply peaked functions like PSFs, by fitting the Fourier transform of the PSF to the Fourier transform of the fitting function, one would be fitting a broad function for which the method of minimization of χ^2 is appropriate.

Before such a program can be undertaken one has to calculate how the $\sqrt{N}$ errors from the PSF photon statistics propagate through the Fourier transform, so that each element of the OTF can be assigned an adequate statistical weight. Due to the linearity of the Fourier transform this calculation is rather straightforward, and the result is surprisingly simple. The derivation is given in the appendix; here we cite only the final result, with $OTF(p,q)$ denoting the value of the (p,q) element of the discrete Optical Transfer Function, and Re, resp. Im, denoting the real resp. imaginary components of the complex matrix elements,

$$[\delta Re(OTF(p,q))]^2 = \frac{Re(OTF(0,0)) + Re(OTF(2p,2q))}{2(2M+1)^2}, \tag{9}$$

and,

$$[\delta Im(OTF(p,q))]^2 = \frac{Re(OTF(0,0)) - Re(OTF(2p,2q))}{2(2M+1)^2}. \tag{10}$$

The wave vectors corresponding to the elements of the discrete OTF are

$$(k_x, k_y) = \frac{(p,q)}{(2M+1)\Delta}, \tag{11}$$

where Δ is the pixel size. We chose to number the grid coordinates in Fourier space (p,q) from $-M$ to M, so that the $\vec{k} = 0$ corresponds to $p = q = 0$. $OTF(p,q)$ is $2M+1$ periodic in p and q, and therefore the argument on the RHS of Eqs. (9) and (10) must be taken modulo $2M+1$. Finally, since the complex OTF is Hermitian (see the Appendix), the number of independent matrix elements is equal to that of the PSF, despite the latter being real.

In conclusion, our procedure is to fit the numerical Fourier transform of the sampled elliptical Moffat function with the OTF, weighted with the inverse of the uncertainties (Eqs. (9) and (10)) derived from photon statistics.

6. Results

6.1 Tabulated Results

We have computed best analytical fits for the preflight measurements of the PSF of the flight configuration Yohkoh Soft X-ray Telescope, obtained with the X-ray laser facility at White Sands Missile Range. The fitting function is the elliptical generalization of the Moffat function, described in Section 4, and the fitting method is that OTF-fitting with photon statistics, described in Section 5 and the appendix.

We fitted 243 single exposures for the SXT PSF (the *bx*-series), and 16 sums of multiple exposures at identical locations (the *sd*-series). These measurements were made at the three wavelengths described above, and at locations distributed over the whole CCD. The original data are available on-line in the Yohkoh data-base, as are the results of our fits, and routines to reconstruct the best analytical fit as a function of position and energy (see Morrison, 1994).

From our list of fitting parameters for the *bx*-series we have excluded two exposures our program could not fit, *bx15_apr24_f.01 and bx51_apr25_f.23*, and all the files in which we noticed "bleeding" in the CCD (caused by over saturation of the image leading to an overflow of electrons from the brightest pixel into neighbouring pixels in the same column). We note that for some of the bleed-affected images, acceptable fits (with, of course, very high eccentricity) were obtained, but chose to eliminate these results so that appropriate parameter averages for the PSF fits can be taken. We have further excluded four exposures, *bx18_apr24_f.04, f.05, f.06*, and *f.07*, for which there is an apparent mistake in the logging of the position of the X-ray source (see Section 6.2).

There remain 216 fits, 62 for the Al-K line, 106 for the C-K line, and 48 for the Ag-L line, for which the fitting results are available on-line (Morrison, 1994), and which we will analyze for trends in the following.

The results for the fitting of the *sd*-series are summarized in Table 1. The parameters given in Table 1 for each measurement are the 8 fitting parameters, the reduced χ^2, the CCD locations of the maximum intensity of the PSF (x_{max} and y_{max}), the X-ray line energy, and, finally, the location of the X-ray point source (x_{source} and y_{source}) in translation stage units (see Section 6.2). The unit for the parameters c and bg (the background) is photon counts (using Eq. (1) on recorded DN), and the unit for x_c, y_c, x_{max}, and y_{max} is the pixel size.

We have omitted from Table 1 the values of the uncertainties in the parameters, calculated from the steepness of the local mimimum in χ^2_ν. These values are typically of the order of a few percent, except for very small values of the parameters x_c, y_c, ε_x, and ε_y, when, as expected, the errors are 100% or larger.

OTF_FIT FOR 25 X 25 PIXEL_FIELD, CENTERED ON PSF-MAX, ELLIPS METHOD, 3/19/93

SXT-IMAGE	A	B	C	Xc	Yc	epsx	epsy	bg	CHI-SQR	Xmax	Ymax	Energy	Xsrc	Ysrc
sd03_apr23_f.01	1.3600	2.3738	40440	0.2863	-0.3052	0.0032	0.0681	125.1	34.19	556	635	Al-K	-7000	-1200
sd04_apr24_f.01	0.7948	1.3880	46863	-0.1891	0.4388	0.5341	-0.1487	56.6	178.02	558	989	Al-K	-7000	2500
sd05_apr24_f.01	0.7355	1.5811	51191	-0.2235	-0.3566	0.2712	0.0396	65.0	9.44	558	268	Al-K	-7000	-5000
sd06_apr24_f.01	0.7079	1.5679	54653	-0.5350	-0.3982	0.3098	0.1287	148.4	14.91	558	268	Al-K	-7000	-5000
sd07_apr24_f.01	1.1095	1.5073	18201	-0.1010	-0.2226	0.3606	0.0830	91.0	45.49	557	121	Al-K	-7000	-6500
sd08_apr24_f.01	0.8415	1.7422	24785	-0.3706	-0.2002	-0.0720	0.0224	85.2	6.68	701	558	Al-K	-5500	-2000
sd14_apr24_f.01	0.7974	1.4643	18308	-0.3889	-0.3896	-0.0626	0.1220	32.2	66.77	265	849	Al-K	-10000	1000
sd16_apr24_f.01	1.2973	2.2770	16105	0.3620	0.1026	0.2562	-0.0071	58.0	23.29	554	412	Al-K	-7000	-3500
sd23_apr24_f.01	0.7825	1.6059	65406	-0.3827	0.0614	-0.0430	0.0975	214.4	11.97	554	634	C-K	-7000	-1200
sd25_apr24_f.01	0.7625	1.4399	52158	-0.4149	0.1785	0.5829	-0.2061	179.4	23.06	554	990	C-K	-7000	2500
sd27_apr24_f.01	1.3045	2.3686	46889	0.2047	-0.4174	0.4608	0.0853	201.8	24.11	554	269	C-K	-7000	-5000
sd30_apr25_f.01	1.5050	2.3665	29922	-0.6045	-0.3869	0.1181	0.2624	183.9	151.74	268	848	C-K	-10000	1000
sd34_apr25_f.01	0.9246	1.9015	53364	0.2272	0.1344	0.1379	0.0846	359.8	11.87	557	410	C-K	-7000	-3500
sd36_apr25_f.01	1.3469	1.7557	22458	0.0725	-0.1323	0.4735	0.0245	211.5	43.34	557	120	C-K	-7000	-6500
sd38_apr25_f.01	1.3592	2.4395	43238	0.1095	-0.1071	0.2517	0.1315	202.8	22.21	701	557	C-K	-5500	-2000
sd40_apr25_f.01	1.1215	2.0613	43669	-0.2684	0.1440	0.3667	0.0477	454.6	7.38	846	410	C-K	-4001	-3500

Table 1. Best elliptical Moffat fits to the WSMR *sd*-files. The *sd*-files are obtained by adding multiple exposures at the same wavelength at identical locations.

6.2 Linearity of Image Formation

As Figure 2 shows, the locations of the maximum intensities form a regular checkerboard pattern over the CCD, with often multiple exposures at the same location. During the measurements the SXT pointing was accomplished with two translation stages. The middle and lower panels of Figure 2 demonstrate the linearity of the image formation (i.e. no image distortion) from the linear relation between the source position, as given by the translation stage (arbitary units), and the location of the center of the PSF. There are only 4 exceptions to this relation, the files in the *bx18*-series mentioned above. Inspection of the fitting parameters leads us to surmise that this is the result of incorrect logging of y_{source}, the y-coordinate of the point source translation stage position. If for these 4 subsequently taken exposures y_{source} does not have the logged value of -3500, but its previous value of -1200, the linear relation is perfectly preserved, except for *bx18_apr24_f.05*, which is an abnormal result overall. Note also that an error in y_{max} is much less likely, since this parameter is not logged during the experiment, but calculated directly from the recorded images. The same linearity in image formation is found for the *sd*-series.

In the remainder of this section we will analyse the results of the fitting procedure, for both the *bx*- and *sd*-series, with emphasis on the variation of parameters and "goodness of fit" with source wavelength, CCD location, and photon number.

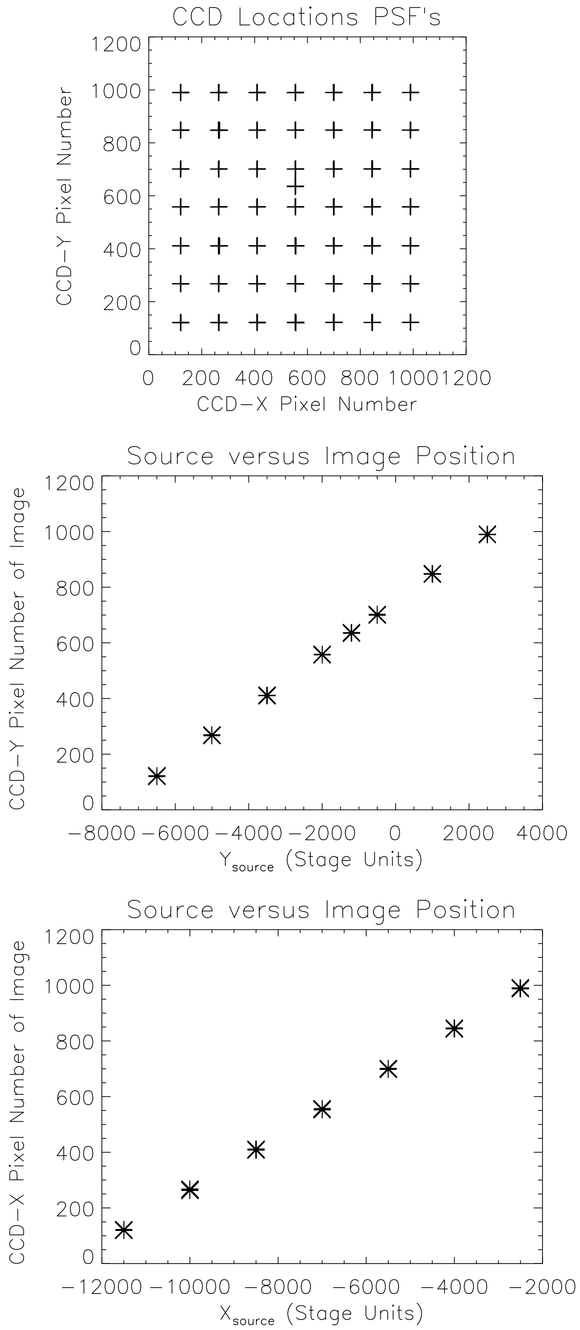

Figure 2. Top: Locations of PSF maxima in the WSMR tests. Middle and bottom: Locations of the x- and y-component of the source position (x_{source}, y_{source}) versus x- and y-location on CCD of PSF maximum (x_{max}, y_{max}).

6.3 Goodness of Fit

First, let us have a look at a typical result. In Fig. 3 we analyze *bx42_apr25_f.19*, centered at $x_{max} = 700$ and $y_{max} = 410$, obtained in the C-K line, and with $\chi^2_\nu = 1.11$. On the bottom we show the PSF and the elliptical Moffat fit obtained with the best fit parameters. The high quality of the fit is obvious. On the top row we show the corresponding contour plots. The latter clearly bring out the elliptical nature of the PSF and the fit. Most other fits are of the same quality. Notable exceptions are the fits near the edge of the CCD, especially the ones in the corners. We will return to this later.

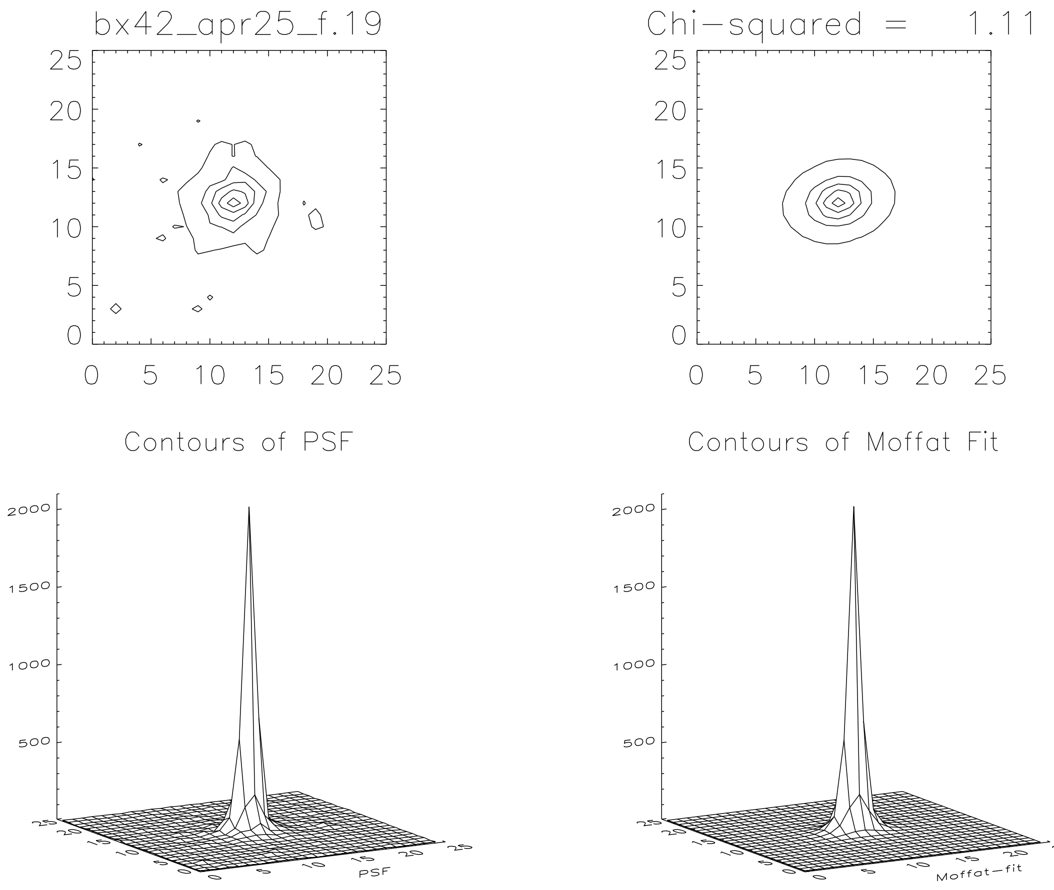

Figure 3. Typical fit of the elliptical Moffat function to a WSMR single exposure near center CCD in the C-K line at 44.7 Å. Shown are surface and contour plots for the PSF and the best fit.

The "goodness of fit" is quantitatively expressed in the reduced χ^2. For cases where the number of degrees of is greater than 100, a χ^2_ν of unity or less represents a statistically "good" fit: that is acceptance level is 48% or better and so the deviations between the experimental results and the analytical fit are not larger, on average, than what is to be expected from the uncertainties in the measurements. An average value of χ^2_ν much less than unity should lead one to caution with regard to the results for the fitting parameters – possibly there is a fairly broad range of parameter values that yield an acceptable value of χ^2_ν of unity or less. An average for χ^2_ν much larger than unity represents an unacceptable fit.

Inspection of the results for the *bx*-series shows that the fits are rather good for all three X-ray lines: the averages of χ^2_ν are 0.29 for the Ag-L line (4.16 Å), 0.86 for Al-K (8.34 Å), and 2.07 for C-K (44.7 Å). There is an obvious tendency here for χ^2_ν to increase with increasing wavelengths, but we ascribe this to a lower error tolerance due to improved photon statistics with increasing wavelength, rather than a less adequate fit by the elliptical Moffat function for longer wavelengths. A comparison of the parameter c (the peak photon count of the Moffat function) for the fits with different wavelengths shows that the average values for Ag-L, Al-K, and C-K are 177, 497, and 1429, respectively.

This trend becomes abundantly clear when comparing with the *sd*-series of Table 1. Here the average of χ^2_ν equals 42.2, with an average c of about 39,000, thus representing large counting statistics. However, the *sd*-files still represent extremely good fits by visual inspection, as Figure 4 bears out for *sd27_apr24_f.01*.

It appears then that the high values of χ^2_ν for the *sd*-files are the result of systematic differences between the measured PSFs and the fitting function, that show up more clearly as the photon statistics improve. For example, let us separate the difference between the PSF and the analytical fit in a photon error and a systematic error, say δ_{ph} and δ_{sys}, respectively. Then $\delta_{ph} \propto \sqrt{N}$, and $\delta_{sys} \propto N$, and the contribution per pixel to χ^2_ν scales as $\delta^2_{sys} + \delta^2_{ph}$. The relative contribution of systematic and photon errors is $\delta^2_{sys}/\delta^2_{ph} \propto N$, so that for large enough photon counts the systematic error will completely dominate. If this is the case for the *sd*-series the ratio of the average χ^2_ν for the *sd*-files and the *bx* C-K line files ($\approx$ 20) should be approximately equal to the ratio of their photon counts, as measured by the parameter c. The result of the latter is $\approx$ 27, indeed close to 20.

The relative error per pixel scales as $\delta_{ph}/\sqrt{N} + \delta_{sys}$, and therefore one expects the relative error to level off to the value of the systematic error for improving photon statistics. The average relative error near the PSF peak for the *sd*-files is about 3% ($\sqrt{\chi^2_\nu/c}$), so we conclude that the analytical fit with the elliptical Moffat function is accurate to about 3%. Therefore the Moffat function is entirely adequate for a representation of the PSF in SXT images obtained in orbit, where the counts are of the order of the peak counts in the *bx*-series, and the corresponding photon statistics lead to uncertainties of several percent.

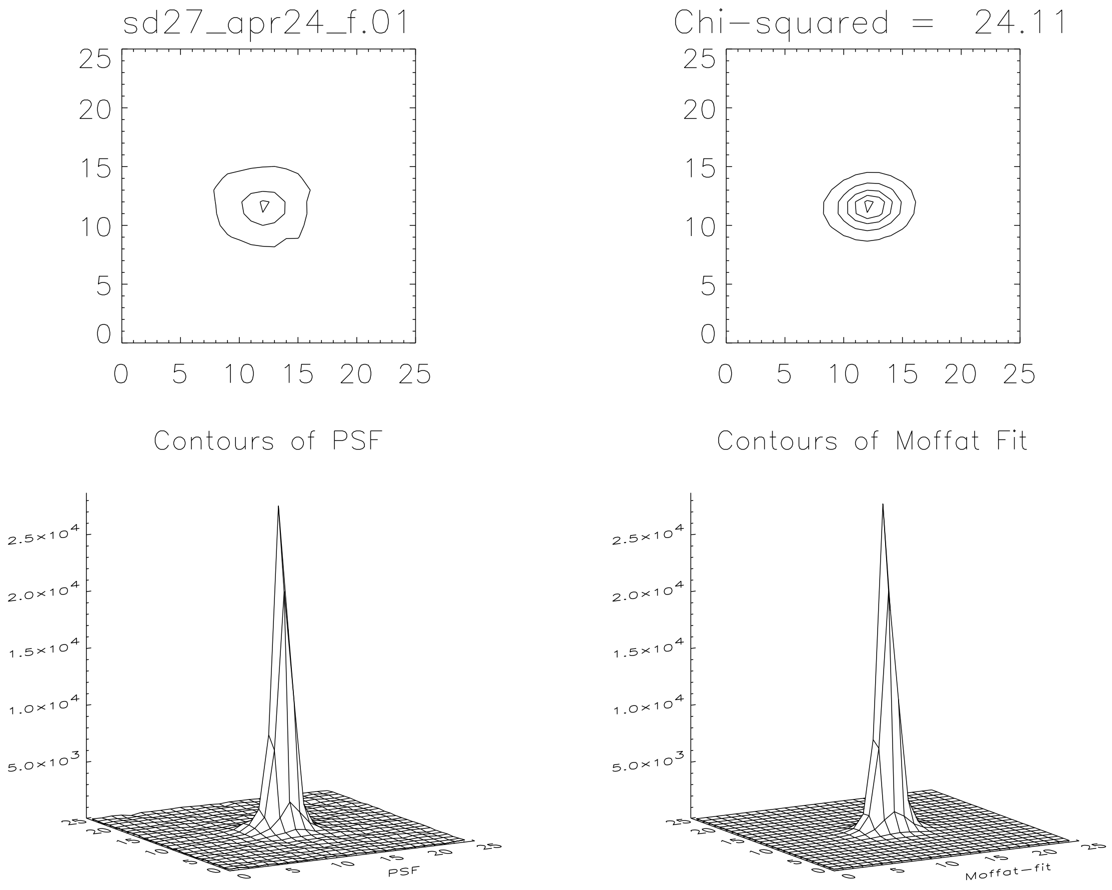

Figure 4. Typical fit of the elliptical Moffat function to a composite of WSMR single exposures at an identical location near center CCD, in the C-K line at 44.7 Å. Shown are surface- and contour plots for the PSF and the best fit.

6.4 Vignetting and FWHM

By far the most irregular PSFs, and the poorest fits, are obtained near the edges of the CCD. If we exclude the outermost columns and rows from the fits (see Fig. 2), we find an average χ^2_ν of 0.21 for Ag-L, 0.53 for Al-K, 1.32 for C-K in the *bx*-series, and 32.0 for the *sd*-series (vs. 0.29, 0.86, 2.07, and 42.2, respectively). The PSFs near the edges, and in particular those in the corners of the CCD are irregular in the sense that they are often double-peaked – a feature that the fitting function cannot deal with – and highly elliptical, much more so than the other PSFs. The latter feature is reproduced adequately in the elliptical Moffat function. Figure 5 shows the PSFs and their best fits for the 4 CCD corner exposures for the C-K line in the *bx21* series. We note that the corner PSFs for the rest of the C-K exposures, and those for the remaining Ag-L and Al-K files, lead to much more irregular fitting results, with often meaningless parameter values.

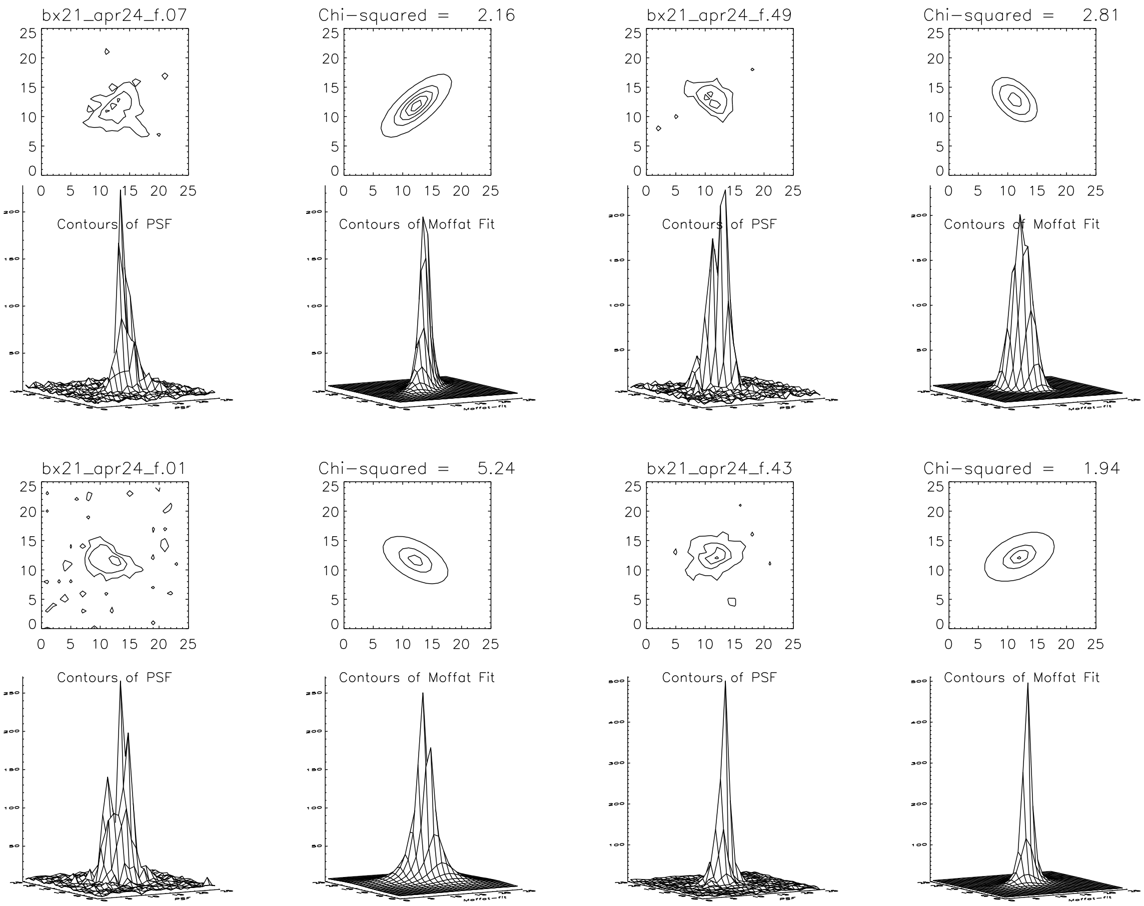

Figure 5. PSF fits at the corners of the CCD for single exposures in the C-K line at 44.7 Å. The plots show clearly the vignetting and irregularity of the PSFs near the edges of the CCD, as well as the poor quality of the Moffat fits.

The orientation of the major axes of the elliptical Moffat function tends to be perpendicular to the direction towards the center of the CCD. In Figure 6 we have plotted for the *bx02*-series vectors with length proportional to the ellipticity, and direction along the major axis at the location of the center of each PSF. The plot clearly shows the trend in direction as well as the increase in ellipticity away from CCD center. The results for the other WSMR experiments are similar. We attribute this result to vignetting, i.e. part of the image becomes obscured by the optics as one moves away from CCD center. Exact ray tracing is needed to determine which part of the optics (e.g. the mirrors or the filter wheels) causes the vignetting. From inspection of the vignetted PSFs it appears that the part turned towards CCD-center of the originally cylindrically symmetric PSF becomes obscured, leading to the elliptical appearance of the PSFs near the edges of the CCD. It is also evident from Fig. 6 that this effect is much larger in the CCD-Y direction than in the CCD-X direction. We have not been able to reach detailed understanding of this asymmetry, but it is possibly to be expected since the instrument is not fully symmetric in the X and Y directions in terms of the filter wheel and aperture stop. We note that from this vignetting one also would expect a decrease in effective area of the SXT with distance from CCD center, a subject that has been investigated elsewhere (Fuller, Lemen, and Acton, 1994).

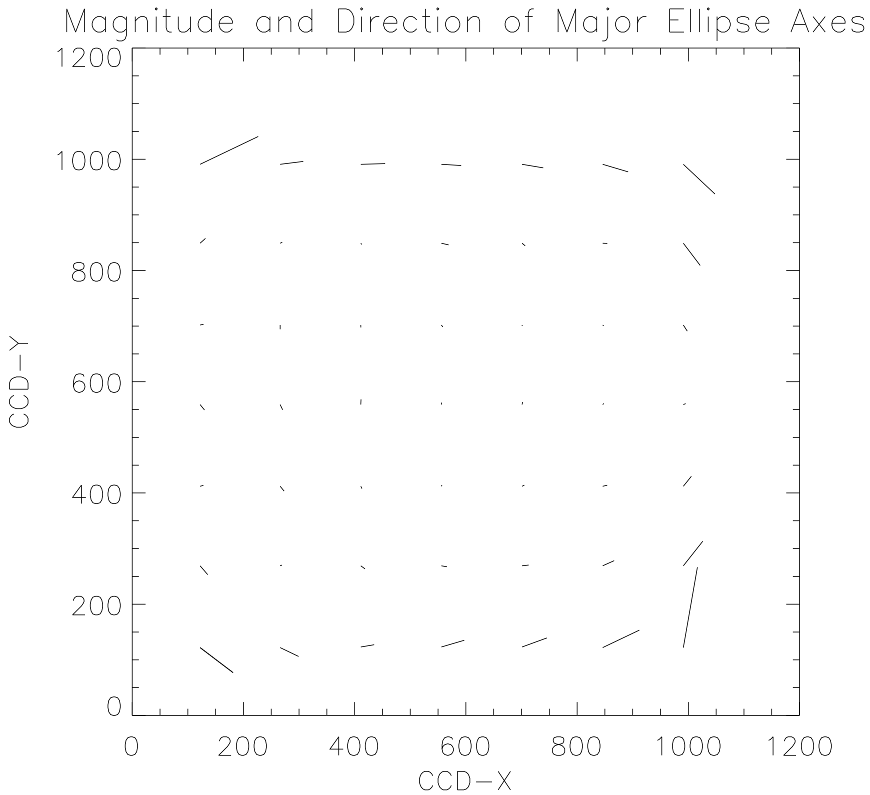

Figure 6. Orientation and relative magnitude of the major axes of the fitted Moffat ellipses as a function of location on the CCD for the *bx02* series of single exposures.

One of the design goals for the SXT (see Lemen *et al,* 1989) was that the FWHM would be fairly constant over the field of view. We have investigated this quantitatively by calculating the FWHM along the long axes of the best fits, given by the expression

$$FWHM \;=\; 2a\sqrt{2^{1/b}-1}. \tag{12}$$

The FWHM along the minor axis of the ellipse is a factor $\sqrt{1+2\varepsilon}$ smaller.

We note that, since the elliptical Moffat function represents a rather good analytical fit for all three wavelengths (except at the edges of the CCD), the determination of the FWHM is quite accurate. This is verified by the results for the uncertainty in the FWHM ($\delta(FWHM)$) calculated from the rules of error propagation,

$$\delta(FWHM) \;=\; \sqrt{(2\sqrt{2^{1/b}-1}\,\delta a)^2} \;+\; \frac{-a\ln(2)2^{1/b}}{b^2\sqrt{2^{1/b}-1}\,\delta b)^2}, \tag{13}$$

which define the error bars in Figure 7.

For each of the three X-ray lines we have calculated the best cubic fit to the FWHM with distance from an arbitrary center of the CCD, with weights assigned according to the uncertainties calculated in Eq. (13) above. From these fits we have excluded all elements located in the outermost columns and rows of Figure 6.

The equation to be fitted is

$$FWHM(r) \;=\; a_0r^3 + a_1r^2 + a_2r + a_3, \tag{14}$$

where r represents the distance to the CCD center,

$$r \;=\; \frac{\sqrt{(a_4 - x_{max})^2 + (a_5 - y_{max})^2}}{500}, \tag{15}$$

which, for convenience, is expressed here in units of 500 pixels. The method used is again χ^2-minimization for adjustment of the parameter vector $\vec{a}$.

The results shown in Figure 7 indicate a spread in the FWHM values larger than can be accounted for from the error bars, and the location of CCD-center is not consistent for the three wavelengths. The corresponding χ^2_ν values are indeed considerably larger than unity. The fitting results are summarized in Table 2. In Table 2 (last column) we have also listed the mean for the FWHM (not weighted) and its standard deviation: there is no systematic increase with wavelength as one might expect.

The parameters a_4 and a_5 in Table 2 represent the optical axis as defined by the minimum FWHM. From these values we find that the average values for X and Y are 537 and 631, respectively. The optical axis has also been determined with reference to the highest reflectivity of the mirror. In that case, values of 515 and 633 were obtained. In both cases, the determinations of these values are not sharply peaked, and so the discrepancy is not as serious as it may seem at first, but it probably is an indication that the mirror has some optical distortion at a low level.

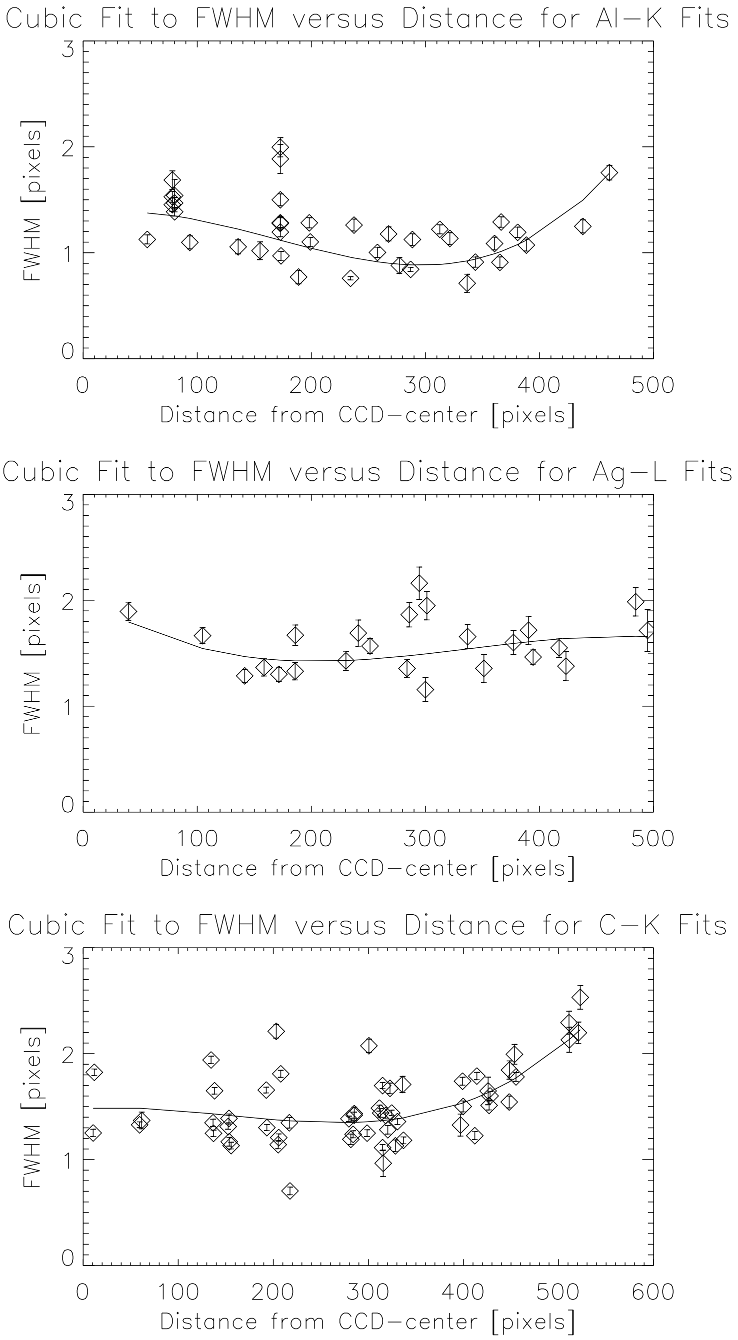

Figure 7. Best fit of FWHM determined from elliptical Moffat fits to a cubic function of distance from the best CCD-center. Separate plots are shown for each X-ray line. The error bars in the FWHM are determined from the uncertainties in the fitting parameters. The drawn line represents the best fit. The numerical results are summarized in Table 2.

We further found that by restricting ourselves to certain subsets of exposures (for example the *bx02* or the *bx51* series) no significantly better results are obtained: the spread of the FWHMs and the values of χ^2_ν remain about the same.

X-Ray	a_0	a_1	a_2	a_3	a_4	a_5	χ^2_ν	Mean FWHM
Wavelength	δa_0	δa_1	δa_2	δa_3	δa_4	δa_5		σ
Ag-L	-3.02	6.14	-3.50	2.03	563	662	5.84	1.59
4.16 Å	0.05	0.04	0.03	0.02	19	9		0.25
Al-K	7.27	-7.32	1.01	1.34	503	577	22.70	1.22
8.34 Å	0.89	1.29	0.58	0.08	6	4		0.30
C-K	2.78	-2.53	0.31	1.48	544	695	44.04	1.52
44.7 Å	0.37	0.50	0.21	0.03	5	8		0.36

Table 2. Cubic fit to FWHM for different wavelengths. Fitting parameters are defined in the text.

6.5 Reproducibility

The results for the FWHM demonstrate a large spread for exposures at identical or very close locations on the CCD. Given the accuracy of the fits, one would expect the PSF and hence the FWHM to be reproducible at identical locations.

OTF_FIT FOR 25 X 25 PIXEL_FIELD, CENTERED ON PSF-MAX, 3/18/93

SXT-IMAGE	A	B	C	Xc	Yc	epsx	epsy	bg	CHI-SQR	Xmax	Ymax	Energy	Xsrc	Ysrc
bx19_apr24_f.01	0.8301	1.6608	491	-0.1543	0.1558	0.0932	0.0554	1.6	0.20	554	412	Al-K	-7000	-3500
bx19_apr24_f.02	1.6493	2.4515	167	-0.2422	0.1426	0.6140	0.0107	1.8	0.22	554	412	Al-K	-7000	-3500
bx19_apr24_f.03	1.1370	1.9188	394	-0.2060	0.1378	0.2625	-0.0265	2.0	0.29	554	412	Al-K	-7000	-3500
bx19_apr24_f.04	0.9210	1.7659	505	-0.2591	0.1375	0.2212	0.0029	2.2	0.20	554	412	Al-K	-7000	-3500
bx19_apr24_f.05	1.7993	2.5842	294	-0.2358	0.1010	0.6209	0.1751	1.6	0.39	554	412	Al-K	-7000	-3500
bx19_apr24_f.06	0.9073	1.7090	454	-0.3166	0.1440	0.1467	0.0711	1.4	0.38	554	412	Al-K	-7000	-3500

Table 3. Best elliptical Moffat fits to a sample of 6 WSMR *bx*-files, obtained at an identical location of the translation stage. These measurements have been used to determine the reproducibility of the PSF measurements.

We have investigated the question of reproducibility in more depth by analyzing the *bx19* series of exposures in the Al-K line, subsequently taken at identical locations of the translation stage, close to the center of the CCD. As Table 3 shows, there is quite a large spread in the fitting parameters: from 0.83 to 1.80 for a, and from 1.66 to 2.58 for b, with the FWHM varying between 1.19 and 2.00. At the same time the values for x_c and x_c (the location in the center pixel of the center of the Moffat function) are very consistent. Since it is very unlikely that the same location would be found 6 times in a row if the real location were not identical, this leads to the conclusion that the source location is indeed very constant. As an aside we remark that this result indicates that it is possible for SXT to determine the location of a point source roughly to within a quarter of a pixel, which is the uncertainty in the position found in our fits.

The question we ask here is whether an arbitrary PSF_1 is consistent with another PSF_2, measured at the identical location, and given the uncertainties from photon statistics. Allowing for different exposure times, we calculate χ^2_ν for the fitting of one measured PSF to another:

$$\chi^2_\nu = \frac{1}{l^2-1}\sum\frac{(\mathrm{PSF}_1-\lambda\mathrm{PSF}_2)^2}{\mathrm{PSF}_1+\lambda\mathrm{PSF}_2}, \tag{16}$$

where l is the pixel length of the matrix over which the fitting takes place (equal to $2M+1$ in Section 2), and where λ is the only fitting parameter, allowing for differences in exposure time. The PSFs have been expressed in photon counts, and the background has been subtracted.

The form of the denominator in Eq. (16) accounts for the fact that the χ^2_ν calculated here relates two datasets, rather than a model and a dataset. The denominator of each term in a χ^2_ν summation represents the square of the uncertainty in each measurement (see Eq. (2)). When taking the difference of two datasets, as is done in the numerator of Eq. (16), there are contributions to the uncertainty from both datasets. Since these contributions are statistically independent, the "sum-of-squares" rule applies, which, in the case where the uncertainty is dominated by photon statistics, leads to the result of Eq. (16).

Since the calculation above is done in real space, the results for χ^2_ν depend strongly on the size of the square fitting matrix l, as was discussed for general fits in Section 2. We found that as we increase l, χ^2_ν decreases, because of the excellent – but meaningless – fit of the outlying regions (with background subtracted) between different sets. Hence we limit ourselves to small l ($l = 5$), so that the majority of pixels considered are well above the background. Indeed the minimum photon count per pixel is around 3.0 for 5 of the PSF measurements considered here, and about 0.5 for *bx19_apr24_f.02*. Hence there is no need to add a constant to the PSFs – as is done in the general Moffat fits – to avoid non-positive counts.

Figure 8 shows one of the results of the fitting of two PSFs, and in Table 4 the cross-correlation matrix for the fitting of the elements of the *bx19*-series is given. The results show that the χ^2_ν are close to unity, with an average of 1.37. We further found, as Figure 8 exemplifies, that the largest deviations (i.e. elements in the summation in Eq. (16)) are consistently near the peak of the PSF, while the fit in the outlying regions is rather good.

The latter result justifies why no parameter allowing for differences in background counts was added to the comparison of Eq. (16). Introducing such a parameter dramatically improves the fits, but the reduction in deviation is mainly near the peaks of the PSFs, where the contribution from the background should be insignificant. Hence the value found for the background counts does not relate to a physical background.

$\chi^2_\nu \setminus \lambda$	1	2	3	4	5	6
1	$\star$	1.97	1.00	0.97	1.03	1.00
2	3.02	$\star$	0.50	0.47	0.53	0.50
3	1.02	0.65	$\star$	0.97	1.03	1.00
4	0.95	0.82	0.65	$\star$	1.07	1.07
5	3.45	0.52	1.26	2.06	$\star$	0.93
6	1.65	0.99	0.90	0.85	1.80	$\star$

Table 4. A cross-correlation matrix of a comparison between PSF measurements in the same wavelength at identical CCD locations. The numbers refer to the last digit of the file name in Table 3. The values for the reduced χ^2 are shown on the lower-left side, those for λ, defined in Eq. (16), on the upper-right side of the matrix.

The conclusion from the comparison in Table 4 is that these PSFs are consistently reproduced to within the error limits set by photon noise. Although it is unsettling that such a large spread in parameters for the fitting function and in FWHMs is found for PSFs that are almost identical to within photon noise, this not unexpected given the small values of χ^2_ν of around 0.3 for these PSFs.

On the positive side we can conclude that for quantitative image analysis of Yohkoh/SXT data the uncertainties derived from photon statistics provide an adequate appoximation.

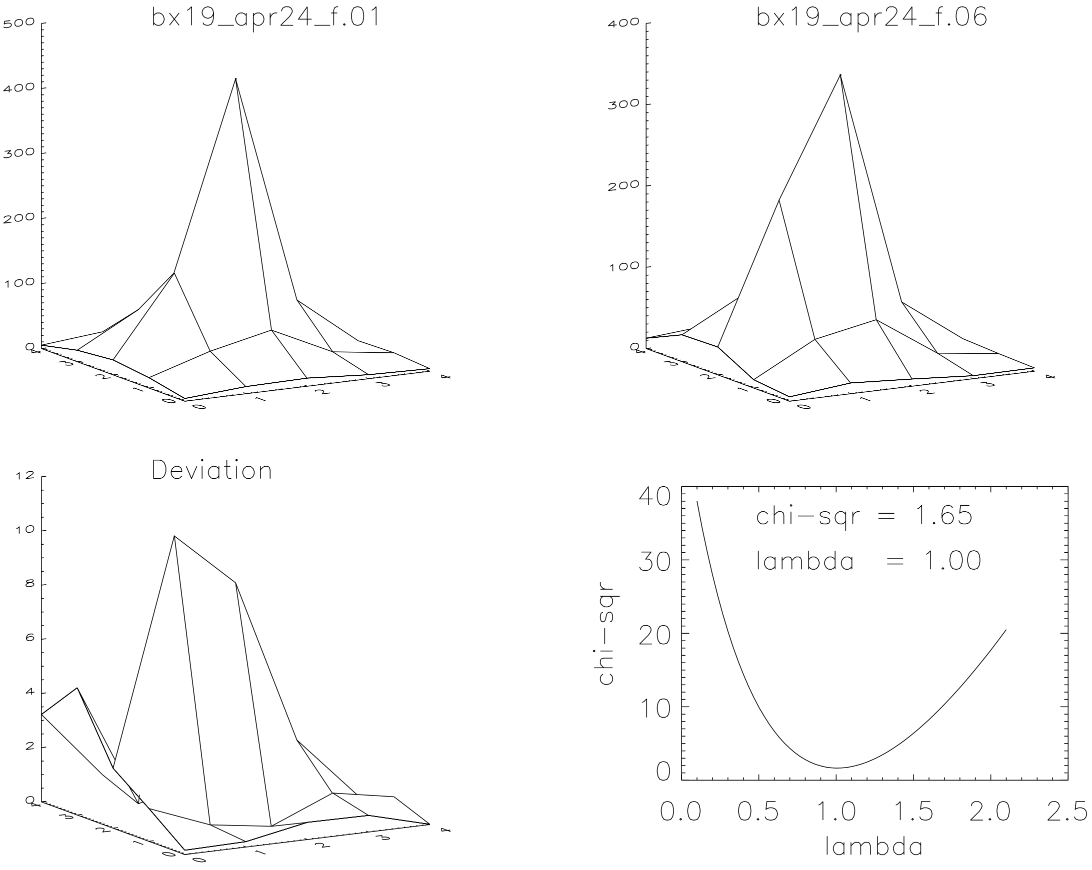

Figure 8. Reproducibility of PSFs measured in the same X-ray line at identical CCD locations. Shown anti-clockwise are two WSMR single exposures at an identical location, and the deviation for each pixel determined from photon statistics. The parameter λ is optimized to minimize the reduced χ^2 as shown in the 4^{th} quadrant.

6.6 Best Analytical Fit

We have analyzed the results for the parameters a and b in the Moffat function, Eq. (5), in the same manner as those for the FWHM (Fig. (7)), and have found no significant trends with position on the CCD when the outermost columns and rows in Fig. 2 were excluded. Therefore we only list the weighted means and standard deviation as a function of wavelength in Table 5. It is obvious that there is no significant trend with wavelength either – in fact the data are consistent with a wavelength independent value for a and b.

The remaining parameters to be determined for a best analytical fit are ε_x and ε_y. Here we take advantage of the result shown in Fig. 6, that the major axes of the elliptical cross-sections of the Moffat function are generally perpendicular to the radius vector from the center of the CCD. In the aproximation that the radius-vector from best CCD center is perpendicular to the ellipse major axis, the parameters ε_x and ε_y can be expressed in terms of the polar angle of the radius vector ϕ, and the absolute value of the ellipticity, denoted by ε. With the help of Eq. (7) for the angle between the x-axis and the major axis of the ellipse we find:

$$\varepsilon_x = -\varepsilon\cos(2\phi) \quad \& \quad \varepsilon_y = -\varepsilon\sin(2\phi). \tag{17}$$

We have fitted ε for all three wavelengths with a cubic fit from best CCD-center as defined in Eqs. (14) and (15), (replace FWHM with ε). The results are summarized in Table 5, and the fit for the C-K line at 44.7 Å is shown in Fig. 9. The histogram of the values of the angle between the radius vector and the direction of the major axis of the elliptical PSF contours, is shown on the right hand side of Fig. 9, and confirms that the ellipse axis tends to be in the azimuthal direction. The ellipticity of the PSF is small near the center of the CCD, but becomes more and more important as one approaches the CCD edges.

This completes the determination of the "best" analytical fit to the SXT PSF. Obviously the parameters c, x_c, and y_c are irrelevant for general image enhancement, but x_c and y_c are quite important if the position of a point source is to be determined with the help of the PSF-fit. Our results are summarized in Table 5, and on-line software is available with the Yohkoh database (Morrison, 1994) to reproduce the best PSF-fits as a function of wavelength and position on the CCD.

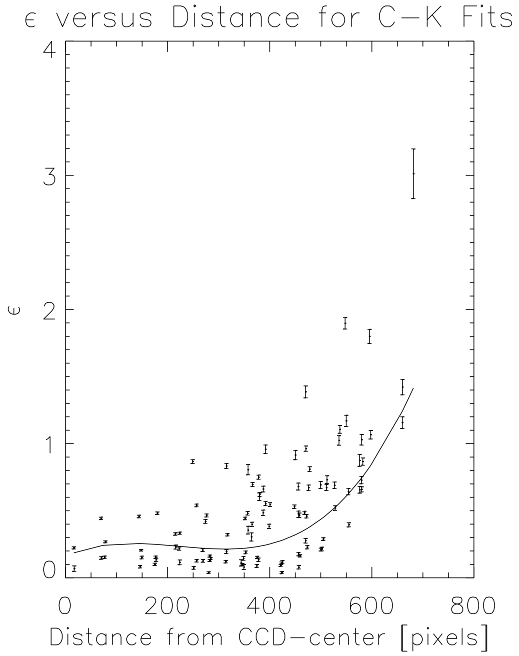

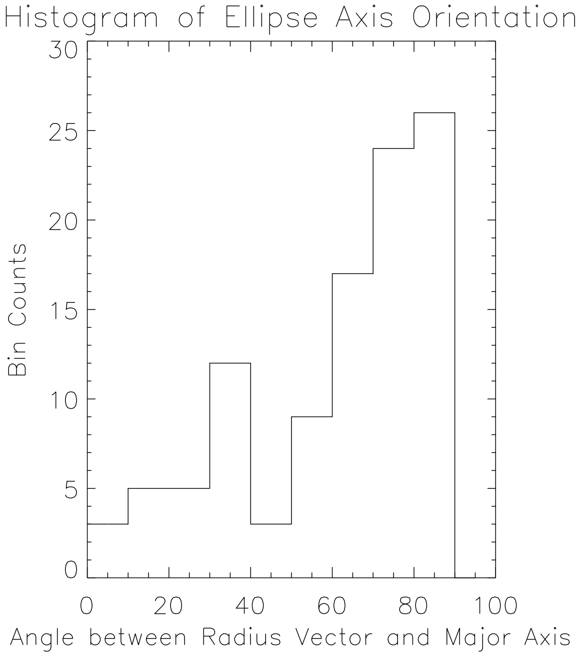

Figure 9. Left: Best cubic fit for the ellipticity of the PSF with distance from best CCD-center in the C-K line at 44.7 $\AA$. Right: Histogram of the angle between the radius vector to best CCD-center and the direction of the major axis of the elliptical PSF contours.

Point Spread Function (r in pixel units)	$PSF(r) \;=\; c/[1+(r/a)^2]^b$	
Elliptical r-contours	$r^2 \;=\; x^2[1+\varepsilon(1+\cos(2\phi))] \;+\; y^2[1+\varepsilon(1-\cos(2\phi))] \;+\; 2\varepsilon\sin(2\phi)xy$	
Location in CCD Coordinates	$x \;=\; x_n - x_{max} - x_c$	$y \;=\; y_m - y_{max} - y_c$
Polar Angle	$\phi \;=\; \arctan(\frac{y_{max}-y_{center}}{x_{max}-x_{center}})$	
Parameters Ag-L @ 4.16 Å Al-K @ 8.34 Å C-K @ 44.7 Å	Mean a 1.10 ± 0.23 0.68 ± 0.24 1.10 ± 0.31	Mean b 1.77 ± 0.24 1.45 ± 0.21 1.85 ± 0.38
CCD-center Ag-L @ 4.16 Å Al-K @ 8.34 Å C-K @ 44.7 Å	x_{center} 536 ± 3 527 ± 2 537 ± 1	y_{center} 591 ± 4 577 ± 2 632 ± 2
Location Dependence of ε Ag-L @ 4.16 Å Al-K @ 8.34 Å C-K @ 44.7 Å	$d^2 \;=\; (x_{max}-x_{center})^2 \;+\; (y_{max}-y_{center})^2$ $\varepsilon \;=\; (2.65 \pm 0.24)d^3 \;-\; (2.99 \pm 0.41)d^2 \;+\; (0.91 \pm 0.21)d \;+\; (0.14 \pm 0.03)$ $\varepsilon \;=\; (2.86 \pm 0.10)d^3 \;-\; (3.96 \pm 0.17)d^2 \;+\; (1.54 \pm 0.09)d \;-\; (0.04 \pm 0.01)$ $\varepsilon \;=\; (1.72 \pm 0.05)d^3 \;-\; (2.29 \pm 0.09)d^2 \;+\; (0.85 \pm 0.04)d \;+\; (0.16 \pm 0.01)$	

Table 5. Summary of the best functional fit for the PSF of Yohkoh's Soft X-ray Telescope determined from the flight configuration tests at White Sands Missile Range. For the three X-ray wavelengths we list the best fitting parameters of the Moffat function and the best parameters for the elliptical deformation of the Moffat function as a function of position on the CCD. The unit of distance is the pixel size.

7. Conclusions

An analytical fit to the SXT Point Spread Function as a function of wavelength and position on the CCD has been derived. The fitting function is the elliptical Moffat function detailed in Table 5. A considerable elliptical deformation of the Moffat function has been found, which increases in magnitude with distance from CCD-center. The major axis of the elliptical contours is directed perpendicular to the radius vector from CCD-center. An analytical expression for this deformation with wavelength dependent parameter values has also been summarized in Table 5. These results will be available on-line in the Yohkoh data-base (Morrison, 1994).

We emphasize that our "best" fit is rather inaccurate at the edges of the CCD, because the White Sands test data show highly irregular, often double-peaked PSFs near the edges. However, in normal operation of SXT, when the center of Sun is projected close to the center of the CCD, these edges are at safe distance from the limb of the X-ray Sun, and therefore do not influence image quality very much.

The fitting method we employed is that of χ^2_ν minimization *in Fourier space* with photon statistics, which we have shown in Section 5 to be the most adequate method for fitting of sharply peaked functions. To make this fitting in Fourier space possible we derived the expression for photon statistics in the Fourier components of an optical image, and of the Optical Transfer Function (OTF) in particular.

By comparing PSF exposures at identical CCD-locations and at identical wavelengths, we found that the uncertainties in these images are within the range expected from photon statistics, which justifies the use of photon statistics in quantitative SXT image analysis. From the same images we determined that SXT can determine the position of a point source with an accuracy of about 1/4 pixel, which is 0.64 arc sec, or about 450 km on the Sun.

The Modulation Transfer Function (the absolute value of the OTF) determined from the Moffat fits shows that there is slight aliasing due to the pixelization at the CCD. This is consistent with the determination of the FWHM for the telescope part of SXT (Lemen *et al.*, 1989), which shows a value less than twice the pixel-size (the Nyquist criterion, see the Appendix).

We note that our determination of the PSF from measuremements at White Sands is relevant for the core of the PSF, not the far wings. Hara *et al.* (1994) have measured the far wings of SXT's PSF from in-flight data. Our results for the PSF have been used in an algorithm for image enhancement implemented for SXT images by LaBonte (1995). The image enhancement routine is available in the Yohkoh analysis system, and an example of image restoration for a set of postflare loops shows a remarkable gain in crispiness of the image (see under *"show-pix"* in the Yohkoh analysis system).

Acknowledgements

We would like to thank the members of the Yohkoh and SXT teams for having made possible this wonderful mission. With regard to the ground tests of the SXT we acknowledge in particular the contributions of William Brown, Marilyn Bruner, Richard Catura, Samuel Freeland, Hugh Hudson, Bruce Jurcevich, Mons Morrison, and Kermit Smith, to whom this paper is dedicated.

The research for this paper was carried out at the Lockheed Solar & Astrophysics Laboratory in Palo Alto, and at ISAS in Tokyo. This work has been supported by NASA under contract NAS 8-37334.

References

Acton, L. W., Lemen, J. R., Brown, W. A., and Morrison, M. 1990, *"SXT Calibration Note 1"*, Lockheed Palo Alto Research Laboratory

Bendinelli, O. 1991, *Ap. J.* **366**, 599.

Bevington, P. R. 1969, *"Data reduction and Error Analysis for the Physical Sciences"*, (McGraw-Hill).

Fuller, R., Lemen, J. R., and Acton, L.W. 1994, *"SXT Calibration Note 37"*, Lockheed Palo Alto Research Laboratory.

Goodman, J. W. 1968, *"Introduction to Fourier Optics"*, Chap. 2, McGraw-Hill Classic Textbook Reissue Series, McGraw-Hill Book Company.

Hara, H., Tsuneta, S. Acton, L. W., Bruner, M., Lemen, J. R., and Ogawara, Y. 1994, *Publ. Astron. Soc. of Japan*, **46**, 493.

LaBonte, B. 1995, in preparation.

Lemen, J. R., Clafflin, E. S., Brown, W. A., Bruner, M. E., Catura, R. C., and Morrison, M. D. 1989, *SPIE*, Vol. **1160**, 316.

Nariai, K. 1987, *Appl. Opt.*, **26**, 4428.

Nariai, K. 1988, *Appl. Opt.*, **27**, 345.

Morrison, M. 1994, *"Yohkoh Analysis Guide"*, To receive a copy, contact by electronic mail on Internet: software@isass0.solar.isas.ac.jp

Ogawara, Y., Takano, T., Kato, T., Kosugi, T., Tsuneta, S., Watanabae, T., Kondo, I., and Uchida, Y. 1991, *Solar Phys.* **136**, 1.

Tsuneta, S., and 12 co-authors 1991, *Solar Phys.* **136**, 37.

Appendix: Photon Statistics for Optical Transfer Functions

Our treatment of the propagation of errors in photon counts through the Fourier transform will be focused on *discrete* transforms; the kind one deals with in numerical and data analysis. However, the generalization to continuous transforms will be obvious.

First we write down the definition of the discrete Fourier transform used in IDL programming language. With f denoting a function in real space, F its Fourier transform, M determining the size of the lattice and (n, m) integers denoting the coordinates of the pixels, as in Section 5, and finally $i = \sqrt{-1}$, we have

$$F_d(p,q) \;=\; \frac{1}{(2M+1)^2}\sum_{n=-M}^{M}\sum_{m=-M}^{M} f_d(n,m)\exp[-\frac{2\pi i(pn+qm)}{2M+1}], \tag{18}$$

where the discrete coordinates of the Fourier matrix (p, q) are integers.

It is evident from the expression above that $F_d(p+(2M+1), q+(2M+1)) = F_d(p,q)$, and therefrom that at most $(2M+1)^2$ independent Fourier components can be calculated from a $(2M+1)^2$ matrix. In addition, by comparing the definition above with the definition of the continuous Fourier transform,

$$F(k_x,k_y) \;=\; \int_{-\infty}^{\infty}\int_{-\infty}^{\infty} f(x,y)\exp[-2\pi i(k_x x+k_y y)]\,dx\,dy \tag{19}$$

it becomes clear that the wave vectors corresponding to the elements of the discrete Fourier transform are

$$(k_x,k_y) \;=\; \frac{(p,q)}{(2M+1)\Delta}, \tag{20}$$

where Δ is the pixel size.

Inverting Eq. (19), and inserting the resulting expression in the definition for the discrete Fourier transform (Eq. 18), with $f_d(n,m)$ denoting a sampled version of $f(x,y)$, one finds, after some straightforward algebra,

$$F_d(p,q) \;=\; \frac{1}{(2M+1)^2\Delta^2}\sum_{j=-\infty}^{\infty}\sum_{l=-\infty}^{\infty} F(k_x-\frac{j}{\Delta}, k_y-\frac{l}{\Delta}), \tag{21}$$

where the relation between (k_x, k_y) and (p, q) is given by Eq. (20).

The above expression clarifies both the *aliasing* phenomenon and the *Nyquist criterion.* The latter follows from the summation in the RHS of Eq. (21): it is evident that only if the continuous Fourier transform $F(k_x, k_y)$ has an effective bandwidth *smaller or equal* than $1/\Delta$ – i.e. its absolute values outside the range $(k_x, k_y) \in [-\frac{1}{2\Delta}, \frac{1}{2\Delta}]$ are negligible – then the elements of the discrete Fourier transform $F_d(p, q)$ correspond to just one wave vector in $F(k_x, k_y)$, and $F_d(p, q)$ is a reliable sample of the continuous transform. The bandwidth of the image $f(x,y)$ is (in our case) the inverse of the resolution of the telescope in front of the CCD, and hence largest pixel-size still conforming to this requirement equals one half of the resolution of the image $f(x,y)$, which is indeed the Nyquist criterion.

Aliasing occurs when the Nyquist criterion is not satisfied: then Eq. (21) indicates that every term in $F_d(p,q)$ consists of a summation of several terms from the continuous transform. Hence, for such an aliased discrete Fourier transform, it is impossible, without any further information, to separate the contribution from different wavevectors in the continuous image $f(x,y)$. A detailed derivation and more extensive discussion is presented in Goodman (1968, Chap. 2).

We will now continue the calculation of the propagation of photon noise through the Fourier discrete transform. For algebraic convenience we split the transform in real $Re(F)$ and imaginary $Im(F)$ components,

$$Re(F_d(p,q)) = \frac{1}{(2M+1)^2} \sum_{n=-M}^{M} \sum_{m=-M}^{M} f_d(n,m) \cos[\frac{2\pi(pn+qm)}{2M+1}], \tag{22}$$

and,

$$Im(F_d(p,q)) = \frac{1}{(2M+1)^2} \sum_{n=-M}^{M} \sum_{m=-M}^{M} f_d(n,m) \sin[\frac{2\pi(pn+qm)}{2M+1}]. \tag{23}$$

Now note that both the real and imaginary components involve a simple summation over the photon count per pixel, $f_d(n,m)$, times a *sine* or *cosine* weighting function, which has no measurement uncertainty. Therefore we can apply the "sum-of-squares" rule – i.e. for $c = \lambda a + \mu b$, with a and b statistically independent measurements, and λ and μ arbitrary constants $(\delta c)^2 = (\lambda \delta c)^2 + (\mu \delta b)^2$ – and use the fact that $(\delta f_d(n,m))^2 = f_d(n,m)$ to find

$$[\delta Re(F_d(p,q))]^2 = \frac{1}{(2M+1)^4} \sum_{n=-M}^{M} \sum_{m=-M}^{M} f_d(n,m) \cos^2[\frac{2\pi(pn+qm)}{2M+1}], \tag{24}$$

and,

$$[\delta Im(F_d(p,q))]^2 = \frac{1}{(2M+1)^4} \sum_{n=-M}^{M} \sum_{m=-M}^{M} f_d(n,m) \sin^2[\frac{2\pi(pn+qm)}{2M+1}]. \tag{25}$$

Using the trigonometric relations $\cos^2\alpha - \sin^2\alpha = \cos 2\alpha$, and $\cos\alpha^2 + \sin\alpha^2 = 1$, the expressions above can be simplified to

$$[\delta Re(F_d(p,q))]^2 = \frac{Re(F_d(0,0)) + Re(F_d(2p,2q))}{2(2M+1)^2}, \tag{26}$$

and,

$$[\delta Im(F_d(p,q))]^2 = \frac{Re(F_d(0,0)) - Re(F_d(2p,2q))}{2(2M+1)^2}. \tag{27}$$

Note that since $F_d(p,q)$ is $2M+1$ periodic in p and q, the argument on the RHS has to be taken modulo $2M+1$.

This result is a surprisingly simple expression for the uncertainty in the real and imaginary components of the Fourier transform of any optical image (in particular the PSF), adequate for use in numerical analysis.

Finally, because the PSF is a real function, its transform, the Optical Transfer Function (OTF), is Hermitian, i.e., if we number the grid coordinates in Fourier space (p,q) from $-M$ to M, then

$$OTF(-p,-q) = OTF^*(p,q). \tag{28}$$

This reduces the number of independent elements of the OTF to $(2M+1)^2$, with in particular $Im[OTF(0,0)] = 0$. In our fitting procedure therefore, χ^2_ν for the OTF, defined in Eq. (4), has the same number of degrees of freedom as the PSF.